

# Geophysical Research Letters

## RESEARCH LETTER

10.1029/2019GL086663

### Key Points:

- We measure and date individual isochronal radar internal reflection horizons across the Weddell Sea sector of the West Antarctic Ice Sheet
- Horizons dated to 1.9–3.2, 3.5–6.0, and 4.6–8.1 ka are widespread and linked to previous radar surveys of the Ross and Amundsen Sea sectors
- These form the basis for a wider database of ice sheet architecture for validating and calibrating ice sheet models of West Antarctica

### Supporting Information:

- Supporting Information S1

### Correspondence to:

D. W. Ashmore,  
d.ashmore@liverpool.ac.uk

### Citation:

Ashmore, D. W., Bingham, R. G., Ross, N., Siegert, M. J., Jordan, T. A., & Mair, D. W. F. (2020). Englacial architecture and age-depth constraints across the West Antarctic Ice Sheet. *Geophysical Research Letters*, 47, e2019GL086663. <https://doi.org/10.1029/2019GL086663>

Received 15 DEC 2019

Accepted 27 FEB 2020

Accepted article online 2 MAR 2020

© 2020. The Authors.

This is an open access article under the terms of the Creative Commons Attribution License, which permits use, distribution and reproduction in any medium, provided the original work is properly cited.

## Englacial Architecture and Age-Depth Constraints Across the West Antarctic Ice Sheet

David W. Ashmore<sup>1</sup> , Robert G. Bingham<sup>2</sup> , Neil Ross<sup>3</sup> , Martin J. Siegert<sup>4</sup> , Tom A. Jordan<sup>5</sup> , and Douglas W. F. Mair<sup>1</sup> 

<sup>1</sup>School of Environmental Sciences, University of Liverpool, Liverpool, UK, <sup>2</sup>School of GeoSciences, University of Edinburgh, Edinburgh, UK, <sup>3</sup>School of Geography, Politics and Sociology, Newcastle University, Newcastle upon Tyne, UK, <sup>4</sup>Grantham Institute and Department of Earth Science and Engineering, Imperial College London, London, UK, <sup>5</sup>British Antarctic Survey, Cambridge, UK

**Abstract** The englacial stratigraphic architecture of internal reflection horizons (IRHs) as imaged by ice-penetrating radar (IPR) across ice sheets reflects the cumulative effects of surface mass balance, basal melt, and ice flow. IRHs, considered isochrones, have typically been traced in interior, slow-flowing regions. Here, we identify three distinctive IRHs spanning the Institute and Möller catchments that cover 50% of West Antarctica's Weddell Sea Sector and are characterized by a complex system of ice stream tributaries. We place age constraints on IRHs through their intersections with previous geophysical surveys tied to Byrd Ice Core and by age-depth modeling. We further show where the oldest ice likely exists within the region and that Holocene ice-dynamic changes were limited to the catchment's lower reaches. The traced IRHs from this study have clear potential to nucleate a wider continental-scale IRH database for validating ice sheet models.

**Plain Language Summary** Ice-penetrating radar is widely used to measure the thickness of ice sheets, critical to assessments of global sea level rise potential. This technique also captures reflections from chemical contrasts within the ice sheet, caused by the atmospheric deposition of conductive impurities, known as “internal reflection horizons” (IRHs) that can be traced over large distances. As these deposits are laid down in distinct events, most IRHs are isochronous age tracers and contain valuable information on past ice sheet processes. In this paper we trace and place age constraints on stratigraphic horizons across a large portion of the West Antarctic Ice Sheet, including regions where fast ice flow has disrupted the ice sheet stratigraphy. The resulting data set allows us to identify where the oldest ice is buried in the study region and provides evidence that flow of the ice sheet interior has been stable during the Holocene. Our results can be used to test the performance of ice sheet models, which seek to simulate the response of ice sheets to long-term environmental change.

## 1. Introduction

Projecting the future of the West Antarctic Ice Sheet (WAIS) and its potential impacts on rising global sea level has developed into a major imperative over recent decades, in response to satellites observing pervasive ice loss (Shepherd et al., 2019) that may indicate the onset (Feldman & Leverman, 2015) of a predicted collapse (Mercer, 1978). However, in order to have confidence in the ice sheet models used to predict such behavior, they must be informed and calibrated by data-driven constraints on ice behavior preceding the observational era. To date, such constraints have primarily been provided by paleoclimatic information drawn from surface-exposure dating, marine sediments and geomorphology, and ice cores (RAISED Consortium, 2014; Steig & Neff, 2018). By contrast, few studies have taken advantage of a valuable paleoclimatic resource that exists across much of Antarctica, namely, the internal stratigraphic architecture of the ice itself that has been sounded across much of the continent by ice-penetrating radar (IPR).

IPR is the primary method by which ice thickness has been measured across Antarctica (e.g., Fretwell et al., 2013). However, most IPR surveys have also sounded numerous englacial internal reflection horizons (IRHs) throughout the ice column (e.g., Steinhage et al., 2001; Winter et al., 2017), and these, away from density-driven reflectivity contrasts in the near-surface (Kovacs et al., 1995), and the strained ice of the basal zone where anisotropic effects become important (Fujita et al., 2000; Wang et al., 2018), are widely attributed

to conductivity variations associated with the atmospheric deposition of impurities at the surface (Bingham & Siegert, 2007; Holschuh et al., 2018; Miners et al., 2002). With the exception of basal ice and erosional surfaces (e.g., Arcone et al., 2012; Cavitte et al., 2016; Holschuh et al., 2018), continuous IRHs can be considered isochronal and hence reflect the advection of paleo-ice surfaces. Consequently, their imaged architecture represents a record of surface mass balance (SMB), basal melt, and ice flow and has the potential to constrain and inform ice sheet models (Hindmarsh et al., 2006; Leysinger Vieli et al., 2011). An archive of IRHs developed recently for the Greenland Ice Sheet from IPR data demonstrates how such data, tied to ice core chronologies, can be used to build spatially distributed age-depth profiles across a polar ice sheet (MacGregor et al., 2015). This resource provides key evidence that ice flow throughout Greenland decelerated during the Holocene (MacGregor et al., 2016). Given the uncertainty that remains regarding the future of the WAIS (Bamber et al., 2019), the development of a similar archive of internal architecture across the WAIS, ultimately tied to ice core chronologies, has been established as an internationally agreed objective (e.g., <https://www.scar.org/science/antarchitecture/home/>).

The Institute and Möller Ice Streams (IMIS) comprises 50% of the total area of the WAIS that discharges to the Weddell Sea via the Filchner-Ronne Ice Shelf. Although not currently identified as a region of major ice loss by satellite altimetry (Shepherd et al., 2019), several recent studies, in part using IPR-sounded IRHs, have posited that the region has hosted significant ice-dynamical changes since the Last Glacial Maximum and through the Holocene (Bingham et al., 2015; Hillenbrand et al., 2014; Kingslake et al., 2016; Siegert et al., 2013; Siegert et al., 2019; Winter et al., 2015). Under climate change in the latter half of the 21st century a reorganization of ocean currents could increase melting considerably in the Filchner-Ronne Ice Shelf cavity (Hellmer et al., 2012), leading to marine ice sheet instability as the bed upstream of the grounding lines dips steeply upglacier (Ross et al., 2012).

We successfully trace three IRHs extensively across IMIS, into the upper part of the Ross Sea Sector of WAIS, and link two of these surfaces to IRHs previously traced across the Amundsen Sea Sector. The geometry of these isochrones reflects the combined effects of ice sheet accumulation, basal melt, and ice flow. We find a broad north-to-south shallowing of IRHs across IMIS reflecting the modern-day SMB gradient and consider evidence for IRH modification due to ice flow and/or basal melting. Placing broad age constraints on the traced IRHs, we infer that postulated Holocene reorganization of ice flow in the Weddell Sea sector was limited inland and that the oldest ice in the catchment underlies the onset region of IMIS. We conclude that the approach applied in this paper comprises a practical and effective method for developing a distributed database of englacial architecture and age-depth control across the wider West Antarctic Ice Sheet.

## 2. Methodology

Our principal data set comprises >25,000 line kilometers of airborne IPR data acquired across IMIS (Figure 1) during the austral season 2010/2011 using the British Antarctic Survey (BAS) Polarimetric radar Airborne Science Instrument (PASIN). Bed echoes from this survey (hereafter the “IMAFI” survey) have been used to map IMIS' subglacial roughness (Rippin et al., 2014) and geomorphology (Rose et al., 2014, 2015), notably revealing a reverse-sloping bed leading into a deep upstream basin that renders IMIS vulnerable to marine ice sheet instability (Ross et al., 2012; Siegert et al., 2016). Englacial IRHs from the same data set have also been analyzed to reveal that major ice flow pathways have switched within IMIS region throughout the Holocene (Bingham et al., 2015; Kingslake et al., 2018; Siegert et al., 2013; Winter et al., 2015), yet none of these previous analyses of englacial layering has traced individual isochrones across the region.

The IMIS IPR survey is well set up to trace IRHs, or isochrones, in three respects. First, the high number of crossovers and series of parallel transects acquired in the nested grid (Figure 1) afford multiple opportunities for linking horizons across intersecting IPR lines. Second, the IMAFI survey included several long profiles extending across the ice divides to Pine Island Glacier and the Ross Sea Sector Ice Streams. These profiles enable IRHs traced through the IMIS IPR data to be linked to IRHs traced through neighboring surveys. Third, the PASIN data acquisition for IMIS operated in two modes: a deep-looking 150 MHz center-frequency, 12 MHz bandwidth chirp mode designed primarily to sound the bed and englacial layering to ice depths of up to 4 km, and a shallower-probing 0.1  $\mu$ s unmodulated pulse mode optimized for sounding englacial layering in the upper few 100 m but also found to be capable of sounding deeper (~2 km, see

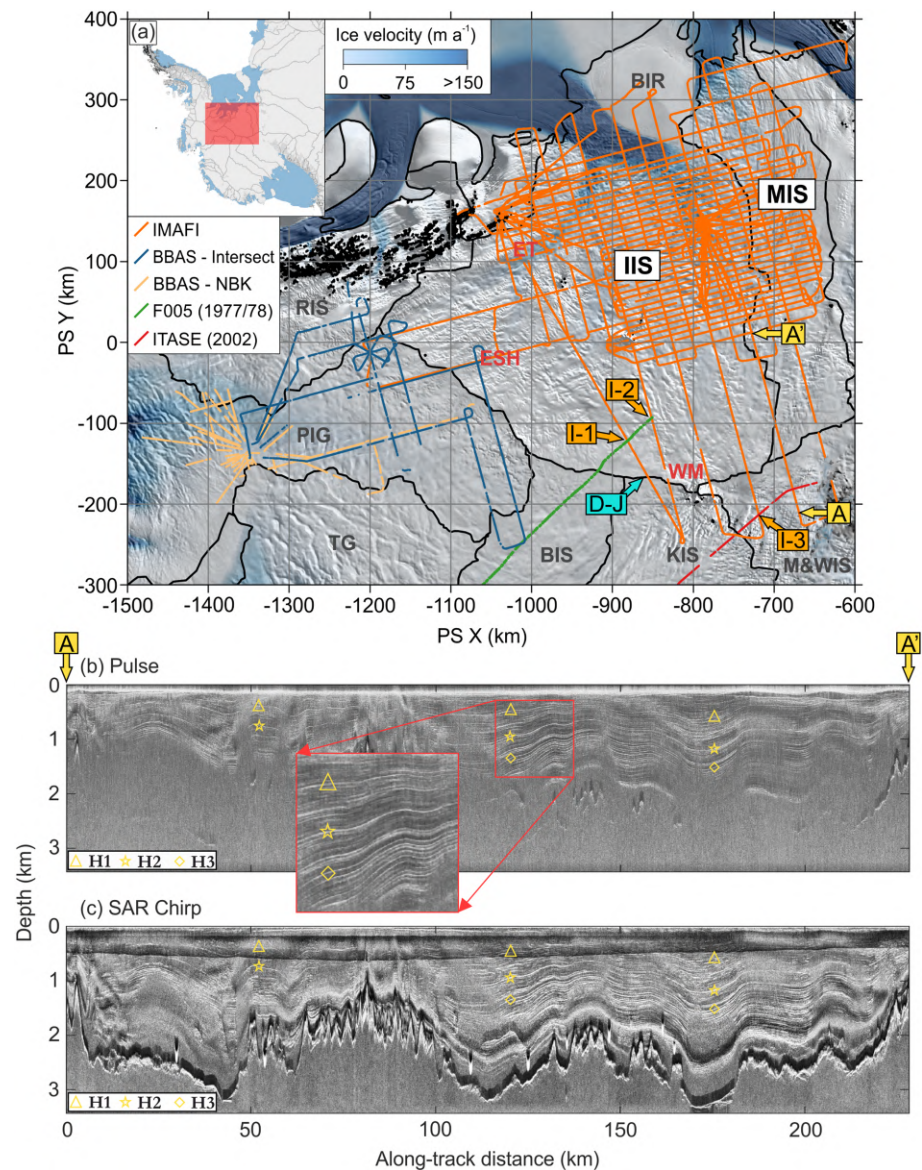


**Figure 1.** (a) The location of our study area (inset), its ice velocity (Mouginot et al., 2019), the data sets used in this study, our control line (A-A'), and major nearby ice catchment and subglacial features. The IPR data sets used in this study include 2010/2011 PASIN survey of IMIS (known as IMAFI); flights from the 2004/2005 PASIN survey of PIG (known as BBAS; Vaughan et al., 2006) which intersect IMAFI (BBAS – Intersect); 2004/2005 PASIN BBAS flightlines in which Karlsson et al. (2014) picked their “layer package” using chirp mode (BBAS – NBK); F005 from the 1977/1978 SPRI-NSF-TUD survey that intersects IMAFI at points I-1 and I-2; and the 2002 ITASE ground survey that intersects IMAFI at point I-3. D-J marks the site where we carry out our age-depth modeling. Ice catchment features: Bungenstock Ice Rise (BIR); Institute Ice Stream (IIS); Möller Ice Stream (MIS); Pine Island Glacier (PIG); Thwaites Glacier (TG); Bindschadler Ice Stream (BIS); Kamb Ice Stream (KIS); and Mercer and Whillans Ice Streams (M&WIS). Subglacial features: Ellsworth Trough (ET); Ellsworth Subglacial Highlands (ESH) and Whitmore Mountains (WM). Background image is MOA (Scambos et al., 2007). Map projection, and for figures herein, is EPSG: 3031. (b) The control line using the unmodulated pulse mode, H1–H3 marked with yellow symbols. (c) The control line using the chirp mode and SAR processing, H1–H3 marked with yellow symbols.

Figure 1b) in the ice. Fuller technical details of the PASIN data are provided by Jeffrey et al. (2018). In a preliminary analysis, we found that both synthetic-aperture radar (SAR)-focused chirp data and the “near-surface” pulse returns were capable of imaging consistent sets of englacial layering through the ice column across much of IMIS (Figure 1).

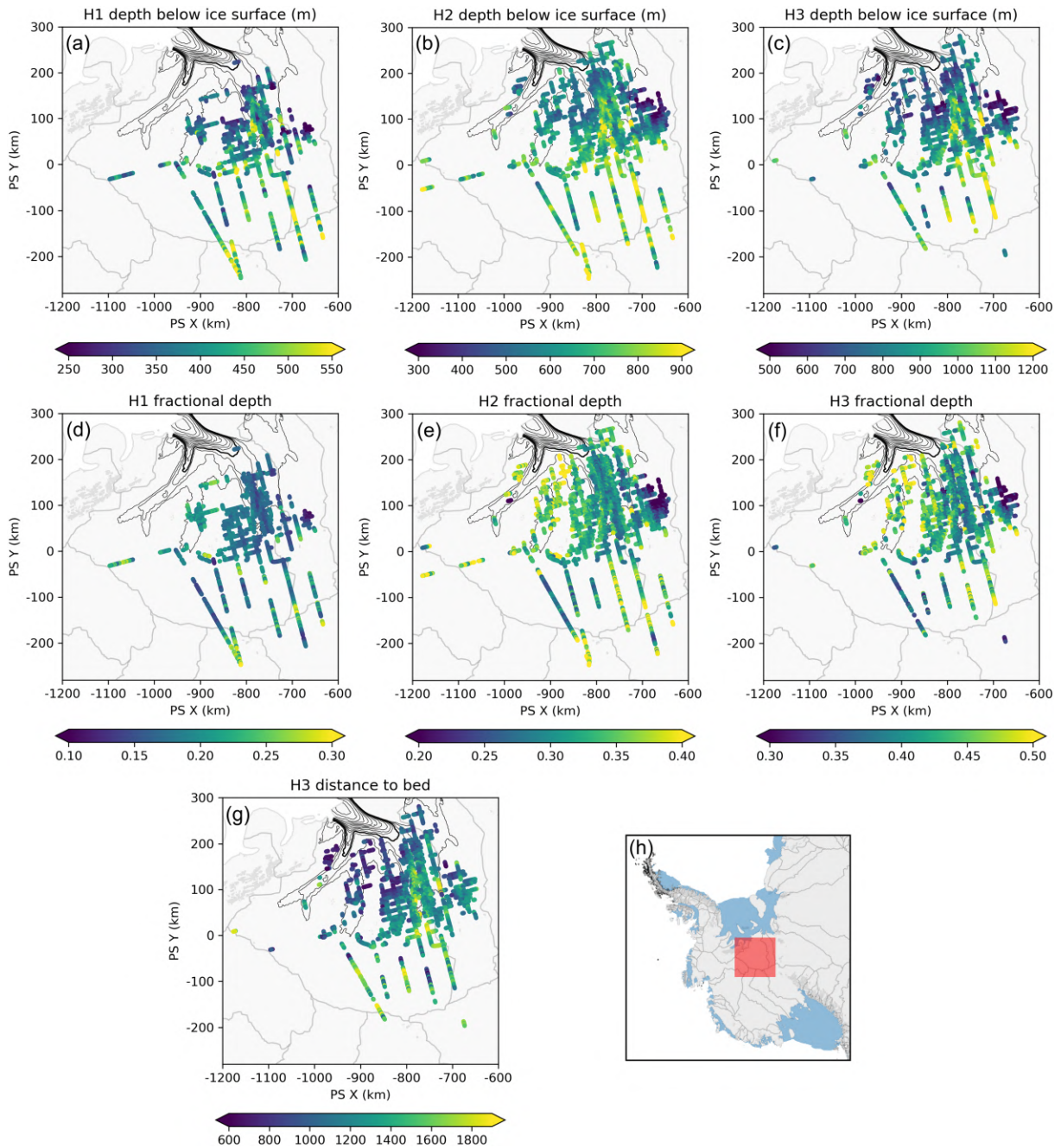


**Figure 2.** Results of the IRH tracking, showing (a–c) depth below surface, (d–f) fractional depth, and (g) the vertical thickness between the deepest IRH, H3, and the bed. Regional ice divides (gray) and  $25 \text{ m a}^{-1}$  ice velocity contours ( $100 \text{ m a}^{-1}$  contour in heavy black) are shown for orientation. (h) Extent of panels (a) to (g).

Our workflow for tracing englacial architecture across IMIS proceeded as follows. The IPR data were first optimized for display by removing the air-to-ice two-way travel time and then applying a custom gain function and a 10-trace horizontal averaging. The data were then converted to the standard 2D SEG-Y-Y format for importing into Schlumberger Petrel®, a 3D visualization and analysis software package designed for seismic data. To begin tracing IRHs, we identified a control IPR line running broadly along flow in the central IMIS catchment from the Weddell-Ross divide in which multiple IRHs are clearly visible (Figure 1). Within this line, and in complementary radargrams produced separately from the chirp and pulse data acquisition, we identified three control IRHs, H1–H3, from as wide a range of depths as possible (Figure 1). H1 and H2,

the shallower IRHs, are the brightest and most traceable IRHs along the control line, but below H2 it is less clear which IRH is most traceable. We elected to pick H3 on the basis that together with H2 it forms a recognizable IRH package analogous to that identified by Karlsson et al. (2014) within Pine Island Glacier. The H2/H3 IRH package bounds a distinct relatively low-reflectivity section of the ice column, with a grouping of closely spaced IRHs in its lower third which can often appear together as a diffuse group (Figure 1). A further diagnostic quality for H3 is that it forms the shallower of a bright couplet of IRHs.

Having traced IRHs H1–H3 along the control line, we progressively traced the same IRHs extending along IPR transects intersecting the control line, moving successively outward from the control line across the survey grid. Tracing typically ceased wherever these IRHs faded out due to steeply dipping reflector geometry or entering disrupted stratigraphy, such that no further clear connection could be made by navigating around intersecting lines or through comparisons with parallel lines. We note that in several areas of IMIS where we have not identified H1–H3, there are IRHs visible in the radargrams that might also be H1–H3, but we did not identify them with the diagnostic criteria outlined above. All resulting IRH picks were converted to depth below the ice surface using an electromagnetic wave speed of  $168.5 \text{ m } \mu\text{s}^{-1}$  (Supporting Information Text S1) and a spatially invariant correction of +10 m to account for the near-surface high-velocity firn layer (Fujita et al., 2000; Dowdeswell & Evans, 2004; Kreutz et al., 2011; see Text S2). We attach a conservative uncertainty of  $\pm 15 \text{ m}$  to our IRH depths arising from the firn correction, IPR system parameters, and variation in electromagnetic wave speed (see Text S3).

To place age constraints on our traced IRHs we examined their intersections with previously dated IRHs derived from earlier airborne and ground-based surveys (see Text S4). Four IRHs traced in a 1977/1978 flight of the Scott Polar Research Institute – National Science Foundation – Technical University of Denmark (SPRI-NSF-TUD) surveys (Siegert et al., 2005) intersect with the IMAFI survey in the upper catchment and are tied to the Byrd Ice Core chronology (Siegert & Payne, 2004). Their ages and stated uncertainties are  $3.1 \pm 0.160 \text{ ka}$ ;  $5.6 \pm 0.175 \text{ ka}$ ;  $6.4 \pm 0.181 \text{ ka}$ ;  $16 \pm 0.324 \text{ ka}$ , arising from an IPR depth resolution of  $\pm 40 \text{ m}$ . Additionally, a deeper reflection in the ITASE traverse, intersecting the IMAFI survey in the upper Mercer/Whillans catchment (Figure 1), was dated to 17.5 ka at Byrd (Jacobel & Welch, 2005). Both the SPRI-NSF-TUD and ITASE data sets were acquired at lower frequency and therefore do not image at the same vertical resolution as the IMAFI survey. To provide an independent validation of these estimated IRH ages we apply a simple accumulation-driven one-dimensional age-depth model after Dansgaard and Johnsen (1969), this model having previously been applied to date IRHs (Fahnestock et al., 2001; Siegert & Payne, 2004; Karlsson et al., 2014). We choose a suitable location on an IMAFI survey line where this model is likely valid (Site D–J in Figure 1a), and a realistic range of values for ice accumulation as informed by contemporary (Arthern et al., 2006; van Wessem et al., 2018) and Holocene (Fudge et al., 2016; Koutnik et al., 2016) estimates, and for basal shear layer thickness (see Text S5). We examine the relationship between our IRHs and those identified in Pine Island Glacier (Text S6) by Karlsson et al. (2014) and the Internal-Layering Continuity Index (ILCI; Karlsson et al., 2012), a proxy for IRH preservation, after Bingham et al. (2015; Text S7).

### 3. Results

Figure 2 shows that H1, H2, and H3 were traceable widely across the IMIS catchments, traversing several of the ice stream tributaries as well as slow-flowing areas in between. Only in the downstream regions of fast flow (surface velocity  $> 100 \text{ m a}^{-1}$ ; representing 4.3% of total IMIS catchment area) did IRH tracing prove impossible, although tracing was also precluded in some areas due to flow being disrupted by significant subglacial protuberances and subglacial mountain ranges (Figure 1). Some variation exists between each IRH in terms of the proportion of the survey tracks in which it is detectable. H1, H2, and H3 were traced in 16%, 31%, and 23% of the survey IPR tracks respectively, but in general, their traceability covers a similar areal distribution, with layering most detectable across the central IMIS region, effectively the onset region of both IIS and MIS (Figure 2). H1 and H2 were also traced along several IPR lines linking over the ice divide into the Mercer/Kamb Ice Stream catchments and H2 also extended into the Pine Island Glacier catchment. The deeper IRHs, H2 and H3, were more readily detectable than H1 nearer to the ice margin, being recoverable across the high ground grid north of Ellsworth Trough (Figure 1) Tributary and extending further than H1 into downstream MIS.

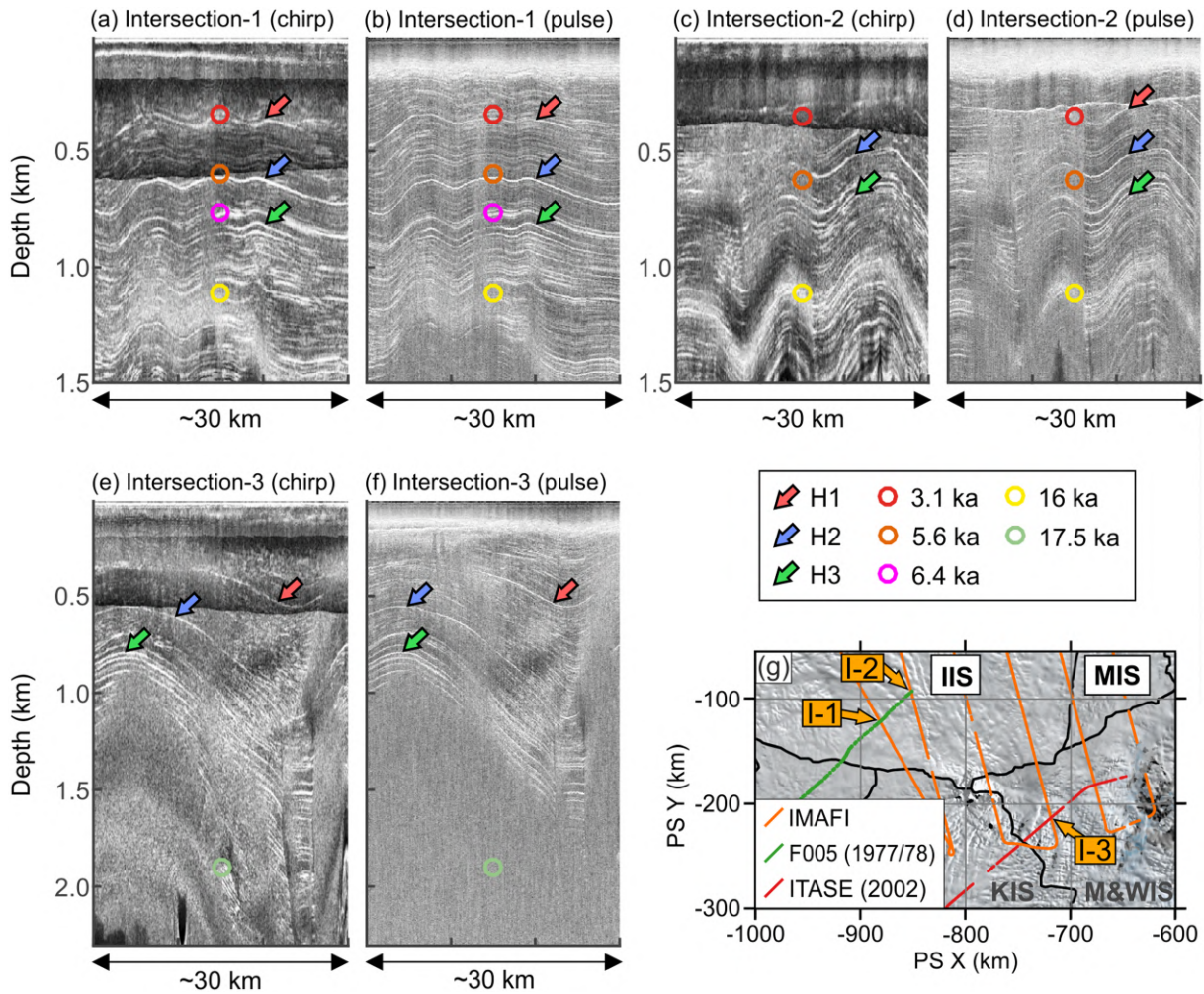
From H1 to H3 respectively, each traced IRH shows greater variability in depth below the ice surface and fraction of ice thickness (where 0/1 is the ice surface/bed). Text S1 and Table S1 provide fuller summary statistics for each IRH. IRHs are notably shallower toward the south of the region and generally the deepest in the ice column over the ice divides (Figure 2). From here, deeper IRHs track into the central IMIS onset zone, corresponding with a deep trough at the ice bed. In Figure 2g we show the distance of our deepest IRH, H3, to the ice bed, demonstrating that up to ~1,700 m of ice exists beneath it.

Figure 3 shows the relationship between our picked layers H1–H3 and the dated IRHs of Siegert and Payne (2004) at two intersections (I-1 and I-2); their relative depths are also provided in Table S2. At I-1, there is a marked correspondence between our IRHs and those of Siegert and Payne (2004), especially considering the unconstrained uncertainties associated with these pioneering surveys (see Text S4). Here (Figures 3a and 3b), H1 and their 3.1 ka layer are vertically offset by 18 m; and H2 and their 5.6 ka layer are offset by 14 m. This is good evidence that the different radar systems both detected the same dielectric contrasts in the ice. At I-2, close to the end of the SPRI-NSF-TUD radargram where there are high levels of clutter and saturation (see Siegert et al., 2005, their Figure 4a), H2 and their 5.6 ka layer are offset by 52 m (Figures 4c and 4d). For deeper IRHs, any correspondence between IRHs is less clear. Siegert and Payne's (2004) 6.4 ka layer broadly corresponds to our H3 (61 m offset at I-1) but lies within a thicker zone of bunched and diffuse reflectors (Figures 3a and 3b). It is not clear which IRHs in the IMIS survey correspond to Siegert and Payne's (2004) 16 ka layer, broadly occurring within a diffuse and smeared zone several hundred meters thick (Figure 3). Figures 3e and 3f show the crossover with the ITASE 2002 survey and the depth of the 17.5 ka layer (Jacobel & Welch, 2005). At I-3, we were only able to trace H1 (385 m depth) and not H2 nor H3 due to slope-induced fading of the returned IPR power at the point of crossover. At I-3, the 17.5 ka layer corresponds to a thick diffuse layer similar to Siegert and Payne's (2004) 16 ka layer (Figures S2f and S2g). This is likely the 17.5 ka IRH which manifests as a bright single reflection in the lower-frequency, lower-resolution ITASE survey.

Our age-depth modeling at Site D-J indicates ages for H1 as 1.9–3.2 ka; H2 as 3.5–6.0 ka; and H3 as 4.6–8.1 ka (Tables S3–S5), consistent with the ages as estimated by the association of the two sets of IRHs at I-1 (Figure 3a). Figures S1 and S2 and Text S1 provide strong evidence that Karlsson et al.'s (2014) “layer package” mapped across Pine Island Glacier is equivalent to the H2 and H3 in this study. Our H2 and H3 are therefore also widespread in the central Pine Island Glacier catchment. From the same workflow we hypothesize that the Siegert and Payne's (2004) 3.1 and 5.6 ka layers are our H1 and H2 and thus that these same layers must extend across Bindshadler Ice Stream and deep into Thwaites Glacier along the SPRI-NSF-TUD flight line.

#### 4. Discussion

Our results demonstrate that, using IPR data acquired with appropriate parameters, englacial architecture can be traced reliably over wide swathes of dynamic ice through West Antarctica. Notably all previous studies exploiting PASIN data to analyze deep echoes (e.g., Bingham et al., 2015; Karlsson et al., 2014) have only used chirp mode. Here we have shown that the PASIN pulsed data acquisition captures englacial architecture at sufficient clarity to allow IRH tracing to ~2 km. This demonstrates a previously unknown utility of the PASIN archive, which covers large parts of West and East Antarctica, for IRH tracing. With reference to the ability to trace IRHs over dynamic ice, almost all previous englacial tracing in Antarctica performed to date has been along or around ice divides, where ice dynamics has not disrupted flow or introduced discontinuities (e.g., Cavitt et al., 2016; Siegert et al., 1998; Siegert et al., 2005; Siegert & Hodgkins, 2000; Winter et al., 2019). Siegert et al. (2005) were able to trace some IRHs across the Siple Coast Ice Streams from the 1970s SPRI-NSF-TUD surveys, but few were traceable across IMIS. Here we have revealed that IRHs (and ultimately paleo-surfaces) can be traced widely across the IMIS catchment, with IRHs reaching almost to the ice margin and IRHs traceable across all but the fastest-flow regions. The greatest challenge to IRH traceability in this region is imposed by ice flow across and/or around significant bedrock obstacles, which is likely to be more acute across IMIS, with its complex subglacial topography (Rippin et al., 2014; Ross et al., 2014) than for other WAIS catchments. The locations of the traceable IRHs correspond well with variations in the ILCI across IMIS derived by Bingham et al. (2015). ILCI is statistically higher where IRHs could be traced in this study (Figure S3 and Text S7). This is the first explicit demonstration of a direct correspondence between



**Figure 3.** IMAFI radargrams and traced IRHs (arrows) at three intersections with published, dated traced IRHs (circles). (g) Locations of the three intersections (I-1, I-2, and I-3), abbreviations and associated references as in Figure 1.

ILCI and manual IRH traceability. This demonstrates that the wider application of ILCI across Antarctic IPR data sets can provide a robust indication of IRH traceability across the ice sheet.

IRH geometry is widely ascribed to the cumulative effect of SMB, ice dynamics, and basal melt (Leysinger Vieli et al., 2011). Mean modeled SMB from 1976 to 2016 (van Wessem et al., 2018) shows a modest increasing SMB gradient from the southern margins of IMIS (see Figure S4), close to the Transantarctic Mountains, to its northern margin and the divide with Pine Island Glacier. Assuming H1 and H2 are accurately dated at I-1, the validity of the local layer approximation (Waddington et al., 2007), and a steady state, we estimate the apparent mean ( $\pm 1$  SD) accumulation across the catchment after MacGregor et al. (2016) since 5.6 ka to be  $0.14 \pm 0.026$  m ice year<sup>-1</sup> (Text S8). Although our implementation of this model is less-constrained than MacGregor et al. (2016), these results and their comparison to regional climate model output provide evidence that the large scale IRH pattern is controlled by SMB (Figure S5). However, considerable spatial heterogeneity and high-frequency variation remain.

As one useful analogue to the possible processes occurring in our study area, Leysinger Vieli et al. (2007) employed an idealized flow-tube model to show the effects that areas of basal slip and basal melt can impose on 3D structure. They showed that IRHs will dip where basal motion transitions from low to high slip. We observe an increase (i.e., deepening) in fractional depth over the IIS tributary in the center of Figures 2d and 2f, which may be due to these effects. An alternative hypothesis for some IRH drawdown along transects that diverge from ice flowlines, such as those depicted in Figure 3, is glacial folding resulting from convergent

flow and ice anisotropy, such as that exemplified by Bons et al. (2016) at the onset of Greenland's Petermann Glacier. IMIS is known to have a complex flow history and packages of basal ice with distinct rheology (Bingham et al., 2015; Ross et al., 2019).

We also see some increase in fractional depth toward the ice divide (Figures 2e and 2f), which cannot be explained by the current flow field. In areas close to the ice divide, where ice flow is currently low, it is unlikely that variations in IRH depth are due to historical ice-dynamic changes as the existing evidence generally supports a stable Holocene WAIS divide (Ross et al., 2011). However, we note that close to South Pole (Beem et al., 2017; Bingham et al., 2007) and in regions of the WAIS (Siegert et al., 2004) some local reorganizations are thought to have occurred and left an imprint on IRH geometry. In the South Pole region such IRH draw-down proximal to an ice divide has been previously attributed to elevated geothermal heat flux (Jordan et al., 2018). Highly radiogenic Jurassic granites which could boost local geothermal heat flux by  $\sim 30 \text{ mW m}^{-2}$ , or 45% to 60% depending on the background heat flux, have been recognized in the Ellsworth Whitmore Mountains region (Leat et al., 2018). Basal melting close to the ice divide could provide an important source of water lubricating the flow of the ice further downstream.

We have placed broad constraints on three IRHs using intersections with previous surveys and age-depth modeling. It is imperative that future work can more directly link these distinctive IRHs with the ice core chronologies at WAIS Divide or Byrd using a modern airborne IPR system. The distance from the deepest, and oldest IRH we trace (H3), and the bed provides an indication of where the oldest ice within the IMIS catchment is. Considering the relative SMB distribution across the WAIS, this is perhaps some of the oldest ice in the WAIS. In the central catchment, for example,  $\sim 1,700 \text{ m}$  of ice older than H3 ( $\sim 6.4 \text{ ka}$ ) exists (Figure 2g). Close to the ice divide,  $\sim 800 \text{ m}$  of ice exists below the 17.5 ka IRH (Jacobel & Welch, 2005; Figures 3e and 3f). Both the 17.5 and 16 ka (after Siegert & Payne, 2004) IRHs are broadly associated with a diffuse region of reflectivity several 100 m thick within IMIS (Ross et al., 2019). Tracing this diffuse zone would further elucidate where thick deposits of ice older than  $\sim 17.5 \text{ ka}$  exist within IMIS. These dates, and the continuity of H3 to within 50 km of the grounding line, imply that the postulated Holocene retreat and readvance of WAIS (Kingslake et al., 2018; Siegert et al., 2013), and its mid-Holocene thinning (Hein, Marrero, et al., 2016), did not have a large effect on the inland portion of this part of the ice sheet. Similarly, the widespread occurrence of these IRHs suggests that the mid-Holocene flow reorganization of the IMIS region (Siegert et al., 2013) was confined to the catchment's lower regions. This supports IPR data suggesting a stable Holocene ice divide (Ross et al., 2011) and longer-term geochronological evidence which points to a relatively stable glaciological system at the WAIS divide over the last 1.4 Ma (Hein, Woodward, et al., 2016).

## 5. Conclusions

Through tracing IRHs along multiple flightlines over a  $210,000 \text{ km}^2$  sector of the WAIS dissected by ice stream tributaries, we have demonstrated that tracing englacial IRHs, and ultimately englacial surfaces, is possible across the wider continental ice sheet. We traced three marker IRHs throughout the upper 50% of the ice column across IIS and MIS using previously underutilized pulsed PASIN IPR data acquired across the catchment in 2010/2011. We used intersections with previous data sets tied to Byrd Ice Core, central West Antarctica, and age-depth modeling to provide broad age constraints of 1.9–3.2 ka, 3.5–6.0 ka, and 4.6–8.1 ka for the IRHs. The IRH configurations across our study region imply that mid-Holocene flow reorganization of the IMIS region was spatially limited. The two lower layers that we traced are very likely the same layers identified by Karlsson et al. (2014) in Pine Island Glacier, providing a direct link to the Amundsen Sea Embayment, while our traced layers also connect into the Ross Sea sector of West Antarctica. By showing that IRHs can be traced across a catchment with a complex ice flow history and well away from ice divides, we have demonstrated encouraging prospects for tracing englacial surfaces extensively and reliably across Antarctica.

## References

- Arcone, S. A., Jacobel, R., & Hamilton, G. (2012). Unconformable stratigraphy in East Antarctica: Part II. Englacial cosets and recrystallized layers. *Journal of Glaciology*, *58*(208), 253–264. <https://doi.org/10.3189/2012JG11J045>
- Arthern, R. J., Winebrenner, D. P., & Vaughan, D. G. (2006). Antarctic snow accumulation mapped using polarisation of 4.3-cm wavelength microwave emission. *Journal of Geophysical Research*, *111*, D06107. <https://doi.org/10.1029/2004JD005667>

### Acknowledgments

D. W. A. would like to thank the Trans-Antarctic Association for Grant TAA-01-19 that allowed him to present and exchange ideas at the 2019 International Glaciological Society Radioglaciology Symposium. Thanks to the editor, Mattieu Morlighem, and Marie Cavitte and Joe MacGregor for their constructive and insightful comments. This paper was stimulated by the AntArchitecture Action Group of the Scientific Committee for Antarctic Research. Mapped IRHs are available online (<https://doi.org/10.5281/zenodo.3635940>). IMAFI IPR data were collected under NERC NE/G013071/1 and available from Siegert et al. (2017).

- Bamber, J. L., Oppenheimer, M., Kopp, R. E., Aspinall, W. P., & Cooke, R. M. (2019). Ice sheet contributions to future sea level rise from structured expert judgement. *Proceedings of the National Academy of Sciences*, *116*(23), 11,195–11,200. <https://doi.org/10.1073/pnas.1817205116>
- Beem, L. H., Cavitte, M. G. P., Blankenship, D. D., Carter, S. P., Young, D. A., Muldoon, G., et al. (2017). Ice-flow reorganization within the East Antarctic Ice Sheet deep interior. *Geological Society, London, Special Publications*, *461*, 35–47. <https://doi.org/10.1144/SP461.14>
- Bingham, R. G., Rippin, D. M., Karlsson, N. B., Corr, H. F. J., Ferraccioli, F., Jordan, T. A., et al. (2015). Ice-flow structure and ice dynamic changes in the Weddell Sea sector of West Antarctica from radar-imaged internal layering. *Journal of Geophysical Research: Earth Surface*, *120*, 655–670. <https://doi.org/10.1002/2014JF003291>
- Bingham, R. G., & Siegert, M. J. (2007). Radio-echo soundings over polar ice masses. *Journal of Environmental and Engineering Geophysics*, *12*(1), 47–62. <https://doi.org/10.2113/JEEG12.1.47>
- Bingham, R. G., Siegert, M. J., Young, D. A., & Blankenship, D. D. (2007). Organized flow from the South Pole to the Filchner-Ronne ice shelf: An assessment of balance velocities in interior East Antarctic using radio echo sounding data. *Journal of Geophysical Research*, *112*, F03S26. <https://doi.org/10.1029/2006JF000556>
- Bons, P. D., Jansen, D., Mundel, F., Bauer, C. C., Binder, T., Eisen, O., et al. (2016). Converging flow and anisotropy cause large-scale folding in Greenland's ice sheet. *Nature Communications*, *7*, 11427. <https://doi.org/10.1038/ncomms11427>
- Cavitte, M. G. P., Blankenship, D. D., Young, D. A., Schroeder, D. M., Parrenin, F., Le Meur, E., et al. (2016). Deep radio stratigraphy of the East Antarctic plateau: Connecting the Dome C and Vostok ice core sites. *Journal of Glaciology*, *62*, 323–334. <https://doi.org/10.1017/jog.2016.11>
- Dansgaard, W., & Johnsen, S. J. (1969). A flow model and a time scale for the ice core from Camp Century, Greenland. *Journal of Glaciology*, *8*(53), 215–223. <https://doi.org/10.3189/S0022143000031208>
- Dowdeswell, J. A., & Evans, S. (2004). Investigations of the form and flow of ice sheets and glaciers using radio-echo sounding. *Reports on Progress in Physics*, *67*(10), 1821–1861. <https://doi.org/10.1088/0034-4885/67/10/R03>
- Fahnestock, M., Abdalati, W., Joughin, I., Brozena, J., & Gogineni, P. (2001). High geothermal heat flow, basal melt, and the origin of rapid ice flow in central Greenland. *Science*, *294*(5550), 2238–2342. <https://doi.org/10.1126/science.1065370>
- Feldman, J., & Leverman, A. (2015). Collapse of the West Antarctic Ice Sheet after a local destabilization of the Amundsen Basin. *Proceedings of the National Academy of Sciences of the United States of America*, *112*, 14,191–14,196. <https://doi.org/10.1073/pnas.1512482112>
- Fretwell, P., Pritchard, H. D., Vaughan, D. G., Bamber, J. L., Barrand, N. E., Bell, R., et al. (2013). Bedmap2: Improved ice bed, surface and thickness data for Antarctica. *The Cryosphere*, *7*, 375–393. <https://doi.org/10.5194/tc-7-375-2013>
- Fudge, T. J., Markle, B. R., Cuffey, K., Buizert, C., Taylor, K. C., Steig, E. J., et al. (2016). Variable relationship between accumulation and temperature in West Antarctica for the past 31,000 year. *Geophysical Research Letters*, *43*, 3795–3803. <https://doi.org/10.1002/2016GL068356>
- Fujita, S., Matsuoka, T., Ishida, T., Matsuoka, K., & Mae, S. (2000). A summary of the complex dielectric permittivity of ice in the megahertz range and its applications for radar sounding of polar ice sheets. In T. Hondoh (Ed.), *Physics of ice core records* (pp. 185–212). Sapporo: Hokkaido University Press.
- Hein, A. S., Marrero, S. M., Woodward, J., Dunning, S. A., Winter, K., Westoby, M. J., et al. (2016). Mid-Holocene pulse of thinning in the Weddell Sea sector of the West Antarctic ice sheet. *Nature Communications*, *7*, 12511. <https://doi.org/10.1038/ncomms12511>
- Hein, A. S., Woodward, J., Marrero, S. M., Dunning, S., Steig, E. J., Freeman, S. P. H. T., et al. (2016). Evidence for the stability of the West Antarctic Ice Sheet divide for 1.4 million years. *Nature Communications*, *7*, 10325. <https://doi.org/10.1038/ncomms10325>
- Hellmer, H. H., Kauker, F., Timmermann, R., Determann, J., & Rae, J. (2012). Twenty-first-century warming of a large Antarctic ice-shelf cavity by a redirected coastal current. *Nature*, *485*(7397), 225–228. <https://doi.org/10.1038/nature11064>
- Hillenbrand, C.-D., Bentley, M. J., Stollard, T. D., Hein, A. S., Kuhn, G., Graham, A. G. C., et al. (2014). Reconstruction of changes in the Weddell Sea sector of the Antarctic Ice Sheet since the Last Glacial Maximum. *Quaternary Science Reviews*, *100*, 111–136. <https://doi.org/10.1016/j.quascirev.2013.07.020>
- Hindmarsh, R. C., Leysinger Vieli, G. J., Raymond, M. J., & Gudmundsson, G. H. (2006). Draping or overriding: The effect of horizontal stress gradients on internal layer architecture in ice sheets. *Journal of Geophysical Research*, *111*, F02018. <https://doi.org/10.1029/2005JF000309>
- Holschuh, N., Christianson, K., Conway, H., Jacobel, R. W., & Welch, B. C. (2018). Persistent tracers of historic ice flow in glacial stratigraphy near Kamb Ice Stream, West Antarctica. *The Cryosphere*, *12*, 2821–2829. <https://doi.org/10.5194/tc-12-2821-2018>
- Jacobel, R. W., & Welch, B. C. (2005). A time marker at 17.5 kyr BP detected throughout West Antarctica. *Annals of Glaciology*, *41*, 47–51. <https://doi.org/10.3189/172756405781813348>
- Jeofry, H., Ross, N., Corr, H. F. J., Li, J., Morlighem, M., Gogineni, P., & Siegert, M. J. (2018). A new bed elevation model for the Weddell Sea sector. *Earth System Science Data*, *10*, 711–725. <https://doi.org/10.5194/essd-10-711-2018>
- Jordan, T. A., Martin, C., Ferraccioli, F., Matsuoka, K., Corr, H., Forsberg, R., et al. (2018). Anomalously high geothermal flux near the South Pole. *Scientific Reports*, *8*(1), 16785. <https://doi.org/10.1038/s41598-018-35182-0>
- Karlsson, N. B., Bingham, R. G., Rippin, D. M., Hindmarsh, R. C. A., Corr, H. F. J., & Vaughan, D. G. (2014). Constraining past accumulation in the central Pine Island Glacier basin, West Antarctica, using radio-echo sounding. *Journal of Glaciology*, *60*, 553–562. <https://doi.org/10.3189/2014JoG13J180>
- Karlsson, N. B. K., Rippin, D. M., Bingham, R. G., & Vaughan, D. G. (2012). A 'continuity index' for assessing ice-sheet dynamics from radar-sounded internal layers. *Earth and Planetary Science Letters*, *335*–336, 88–94. <https://doi.org/10.1016/j.epsl.2012.04.034>
- Kingslake, J., Martin, C., Arthern, R. J., Corr, H. F. J., & King, D. C. (2016). Ice-flow reorganization in West Antarctica 2.5 kyr ago dated using radar-derived englacial flow velocities. *Geophysical Research Letters*, *43*, 9103–9112. <https://doi.org/10.1002/2016GL070278>
- Kingslake, J., Scherer, R. P., Albrecht, T., Coenen, J., Powell, D., Reese, R., et al. (2018). Extensive retreat and re-advance of the West Antarctic Ice Sheet during the Holocene. *Nature*, *558*(7710), 430–434. <https://doi.org/10.1038/s41586-018-0208-x>
- Koutnik, M. R., Fudge, T. J., Conway, H., Waddington, E. D., Neumann, T. A., Cuffey, K. M., et al. (2016). Holocene accumulation and ice flow near the West Antarctic Ice Sheet Divide ice core site. *Journal of Geophysical Research: Earth Surface*, *121*, 907–924. <https://doi.org/10.1002/2015JF003668>
- Kovacs, A., Gow, A., & Morey, R. M. (1995). The in-situ dielectric constant of polar revisited. *Cold Regions Science and Technology*, *23*, 245–256. [https://doi.org/10.1016/0165-232X\(94\)00016-Q](https://doi.org/10.1016/0165-232X(94)00016-Q)
- Kreutz, K., Koffman, B., Breton, D., & Hamilton, G. (2011). *Microparticle, conductivity, and density measurements from the WAIS divide deep ice core, Antarctica*. Boulder, CO: National Snow and Ice Data Center. <https://doi.org/10.7265/N5K07264>

- Leat, P. T., Jordan, T. A., Flowerdew, M. J., Riley, T. R., Ferraccioli, F., & Whitehouse, M. J. (2018). Jurassic high heat production granites associated with the Weddell Sea rift system, Antarctica. *Tectonophysics*, 722, 249–264. <https://doi.org/10.1016/j.tecto.2017.11.011>
- Leysinger Vieli, G. J.-M. C., Hindmarsh, R. C. A., & Siegert, M. J. (2007). Three-dimensional influences on radar layer stratigraphy. *Annals of Glaciology*, 46, 22–28. <https://doi.org/10.3189/172756407782871729>
- Leysinger Vieli, G. J.-M. C., Hindmarsh, R. C. A., Siegert, M. J., & Bo, S. (2011). Time-dependence of the spatial pattern of accumulation rate in East Antarctica deduced from isochronic radar layers using a 3-D numerical ice flow model. *Journal of Geophysical Research*, 116, F02018. <https://doi.org/10.1029/2010JF001785>
- MacGregor, J. A., Colgan, W. T., Fahnestock, M. A., Mörlighem, M., Catania, G. A., Paden, J. D., & Gogineni, S. P. (2016). Holocene deceleration of the Greenland Ice Sheet. *Science*, 352, 590–593. <https://doi.org/10.1126/science.aab1702>
- MacGregor, J. A., Fahnestock, M. A., Catania, G., Paden, J. D., Gogineni, S. P., Young, S. K., et al. (2015). Radiostratigraphy and age structure of the Greenland Ice Sheet. *Journal of Geophysical Research: Earth Surface*, 120, 212–241. <https://doi.org/10.1002/2014JF003215>
- Mercer, J. H. (1978). West Antarctic Ice Sheet and CO<sub>2</sub> greenhouse effect: A threat of disaster. *Nature*, 271, 321–325. <https://doi.org/10.1038/271321a0>
- Miners, W., Wolff, E., Moore, J., Jacobel, R., & Hempel, L. (2002). Modeling the radio echo reflections inside the ice sheet at Summit, Greenland. *Journal of Geophysical Research*, 107(B8), 2172. <https://doi.org/10.1029/2001JB000535>
- Mouginot, J., Rignot, E., & Scheuchl, B. (2019). Continent-wide, interferometric SAR phase mapping, of Antarctic ice velocity. *Geophysical Research Letters*, 46, 9710–9718. <https://doi.org/10.1029/2019GL083826>
- Steig, E. J., & Neff, P. D. (2018). The prescience of paleoclimatology and the future of the Antarctic Ice Sheet. *Nature Communications*, 9(1), 2730. <https://doi.org/10.1038/s41467-018-05001-1>
- RAISED Consortium, Bentley, M. J., Cofaigh, C. O., Anderson, J. B., Conway, H., Davies, B., Graham, A. G., et al. (2014). A community based geological reconstruction of Antarctic Ice Sheet deglaciation since the Last Glacial Maximum. *Quaternary Science Reviews*, 100, 1–9. <https://doi.org/10.1016/j.quascirev.2014.06.025>
- Rippin, D., Bingham, R., Jordan, T., Wright, A., Corr, H. F. J., Ferraccioli, F., et al. (2014). Basal roughness of the Institute and Möller Ice Streams, West Antarctica: Process determination and landscape interpretation. *Geomorphology*, 214, 139–147. <https://doi.org/10.1016/j.geomorph.2014.01.021>
- Rose, K. C., Ross, N., Bingham, R. G., Corr, H. F. J., Ferraccioli, F., Jordan, T. A., et al. (2014). A temperate former West Antarctic Ice Sheet suggested by an extensive zone of subglacial meltwater channels. *Geology*, 42(11), 971–974. <https://doi.org/10.1130/G35980.1>
- Rose, K. C., Ross, N., Jordan, T. A., Bingham, R. G., Corr, H. F. J., Ferraccioli, F., et al. (2015). Ancient pre-glacial erosion surfaces preserved beneath the West Antarctic Ice Sheet. *Earth Surface Dynamics*, 3, 139–152. <https://doi.org/10.5194/esurf-3-139-2015>
- Ross, N., Bingham, R. G., Corr, H. F. J., Ferraccioli, F., Jordan, T. A., Le Brocq, A., et al. (2012). Steep reverse bed slope at the grounding line of the Weddell Sea sector in West Antarctica. *Nature Geoscience*, 5, 393–396. <https://doi.org/10.1038/ngeo1468>
- Ross, N., Corr, H., & Siegert, M. (2019). Large-scale englacial folding and deep-ice stratigraphy within the West Antarctic Ice Sheet. *The Cryosphere Discuss*, in review. <https://doi.org/10.5194/tc-2019-245>
- Ross, N., Jordan, T. A., Bingham, R. G., Corr, H. F. J., Ferraccioli, F., Le Brocq, A., et al. (2014). The Ellsworth subglacial highlights: Inception and retreat of the West Antarctic Ice Sheet. *Geological Society of America Bulletin*, 126, 3–15. <https://doi.org/10.1130/B30794.1>
- Ross, N., Siegert, M. J., Woodward, J., Smith, A. M., Corr, H. F. J., Bentley, M. J., et al. (2011). Holocene stability of the Amundsen-Weddell ice divide, West Antarctica. *Geology*, 39(10), 935–938. <https://doi.org/10.1130/G31920.1>
- Scambos, T., Haran, T., Fahnestock, M., Painter, T., & Bohlander, J. (2007). MODIS-based Mosaic of Antarctica (MOA) data sets: Continent-wide surface morphology and snow grain size. *Remote Sensing of Environment*, 2-3, 242–257. <https://doi.org/10.1016/j.rse.2006.12.020>
- Shepherd, A., Ivins, E., Rignot, E., Smith, B., van den Broeke, M., Veliconga, I., & The IMBIE team (2019). Mass balance of the Antarctic Ice Sheet from 1992 to 2017. *Nature*, 558, 219–222. <https://doi.org/10.1038/s41586-018-0179-y>
- Siegert, M., Jeofry, H., Corr, H., Ross, N., Jordan, T., Ferraccioli, F., et al. (2017). *Synthetic-aperture radar (SAR) processed airborne radio-echo sounding data from the Institute and Möller ice streams, West Antarctica, 2010-11*. UK: Polar Data Centre, Natural Environment Research Council. <https://doi.org/10.5285/8a975b9e-f18c-4c51-9bdb-b00b82da52b8>
- Siegert, M., Ross, N., Corr, H., Kingslake, J., & Hindmarsh, R. (2013). Late Holocene ice-flow reconfiguration in the Weddell Sea sector of West Antarctica. *Quaternary Science Reviews*, 78, 98–107. <https://doi.org/10.1016/j.quascirev.2013.08.003>
- Siegert, M. J., & Hodgkins, R. (2000). A stratigraphic link across 1100 km of the Antarctic Ice Sheet between the Vostok ice core site and Titan Dome (near South Pole). *Geophysical Research Letters*, 27, 2133–2136. <https://doi.org/10.1029/2000GL008479>
- Siegert, M. J., Hodgkins, R., & Dowdeswell, J. A. (1998). A chronology for the Dome C deep ice-core site through radio-echo layer correlation with the Vostok ice core. *Geophysical Research Letters*, 25, 1019–1022. <https://doi.org/10.1029/98GL00718>
- Siegert, M. J., Kingslake, J., Ross, N., Whitehouse, P. L., Woodward, J., Jamieson, S. S. R., et al. (2019). Major ice sheet change in the Weddell Sea Sector of West Antarctic over the last 5000 years. *Reviews of Geophysics*, 57, 1197–1223. <https://doi.org/10.1029/2019RG000651>
- Siegert, M. J., & Payne, A. J. (2004). Past rates of accumulation in central West Antarctica. *Geophysical Research Letters*, 31, L12403. <https://doi.org/10.1029/2004GL020290>
- Siegert, M. J., Pokar, M., Dowdeswell, J. A., & Benham, T. (2005). Radio-echo layering in West Antarctica: A spreadsheet database. *Earth Surface Processes and Landforms*, 30, 1583–1591. <https://doi.org/10.1002/esp.1238>
- Siegert, M. J., Ross, N., Li, J., Schroeder, D. M., Rippin, D., Ashmore, D., et al. (2016). Subglacial controls on the flow of the Institute Ice Stream, West Antarctica. *Annals of Glaciology*, 57, 19–24. <https://doi.org/10.1017/aog.2016.17>
- Siegert, M. J., Welch, B., Morse, D., Vieli, A., Blankenship, D. D., Joughin, I., et al. (2004). Ice flow direction change in interior West Antarctic. *Science*, 305, 1948–1951. <https://doi.org/10.1126/science.1101072>
- Steinhage, D., Nixdorf, U., Meyer, U., & Miller, H. (2001). Subglacial topography and internal structure of central and western Dronning Maud Land, Antarctica, determined from airborne radio echo sounding. *Journal of Applied Geophysics*, 47(3-4), 183–189. [https://doi.org/10.1016/S0926-9851\(01\)00063-5](https://doi.org/10.1016/S0926-9851(01)00063-5)
- Vaughan, D. G., Corr, H. F. J., Ferraccioli, F., Frearson, N., O'Hare, A., Mach, D., et al. (2006). New boundary conditions for the West Antarctic Ice Sheet: Subglacial topography beneath Pine Island Glacier. *Geophysical Research Letters*, 33, L09501. <https://doi.org/10.1029/2005GL025588>
- Waddington, E. D., Neumann, T. A., Koutnik, M. R., Marshall, H.-P., & Moore, D. L. (2007). Inference of accumulation-rate patterns from deep layers in glaciers and ice sheets. *Journal of Glaciology*, 53(183), 694–712. <https://doi.org/10.3189/002214307784409351>

- Wang, B., Sun, B., Ferrocchioli, F., Martin, C., Steinhage, D., Cui, X., & Siegert, M. J. (2018). Summit of the East Antarctic Ice Sheet underlain by extensive thick ice-crystal fabric layers formed by glacial-interglacial environmental change. *Geological Society, London, Special Publications*, *461*, 131–144. [https://doi.org/10.1144/SP461.1\(2018\)](https://doi.org/10.1144/SP461.1(2018))
- van Wessem, J. M., van de Berg, W., Noël, B. P. Y., van Meijgaard, E., Amory, C., Birnbaum, G., et al. (2018). Modelling the climate and surface mass balance of polar ice sheets using RACMO2 – Part 2: Antarctica (1979–2016). *The Cryosphere*, *12*, 1479–1498. <https://doi.org/10.5194/tc-12-1479-2018>
- Winter, A., Steinhage, D., Arnold, E. J., Blankenship, D. D., Cavitte, M. G. P., Corr, H. F. J., et al. (2017). Comparison of measurements from different radio-echo sounding systems and synchronisation with the ice core at Dome C, Antarctica. *The Cryosphere*, *11*, 653–668. <https://doi.org/10.5194/tc-11-653-2017>
- Winter, A., Steinhage, D., Creyts, T. T., Kleiner, T., & Eisen, O. (2019). Age stratigraphy in the East Antarctic Ice Sheet inferred from radio-echo sounding horizons. *Earth System Science Data*, *11*, 1069–1081. <https://doi.org/10.5194/essd-11-1069-2019>
- Winter, K., Woodward, J., Ross, N., Dunning, S. A., Bingham, R. G., Corr, H. F. J., & Siegert, M. (2015). Airborne radar evidence for tributary flow switching in Institute Ice Stream, West Antarctica: Implications for ice sheet configuration and dynamics. *Journal of Geophysical Research: Earth Surface*, *120*, 1611–1625. <https://doi.org/10.1002/2015JF003518>

*Geophysical Research Letters*

Supporting Information for:

**Englacial architecture and age-depth constraints across the West Antarctic Ice Sheet**

David W. Ashmore<sup>1</sup>, Robert G. Bingham<sup>2</sup>, Neil Ross<sup>3</sup>, Martin J. Siegert<sup>4</sup>, Tom A. Jordan<sup>5</sup>,  
Douglas W. F. Mair<sup>1</sup>

*1 – School of Environmental Sciences, University of Liverpool, Liverpool, L69 7ZT, UK; 2 – School of GeoSciences, University of Edinburgh, Drummond Street, Edinburgh, EH8 9XP, UK; 3 – School of Geography, Politics and Sociology, Newcastle University, Newcastle upon Tyne, NE1 7RU, UK; 4 – Grantham Institute and Department of Earth Science and Engineering, Imperial College London, London SW7 2AZ, UK; 5 – British Antarctic Survey, High Cross, Madingley Road, Cambridge, CB3 0ET, UK.*

**Contents of this file**

Supporting Text S1-S8. Supporting Figures S1-S3. Supporting Tables S1-S5

**Introduction**

This file contains supporting information for the Main Text of the above paper. Text S1 details the method used to convert internal reflection horizon (IRH) picks to depth beneath the ice surface, and their summary statistics (Table S1). Text S2 describes the rationale for the firn correction, and S3 describes the estimation of IRH depth uncertainty. Text S4 (and Table S2) outlines how depths were calculated at intersections between IMAFI and previously traced, dated IRHs, and what those depths are. Text S5 describes the age-depth modeling, the justification for the input parameters, and the results (Tables S3, S4, S5). Text S6 (and

Figures S1 and S2) shows the comparison between IMAFI, BBAS flights which intersect IMAFI and the “layer package” identified by Karlsson et al. (2014) in the BBAS chirp data. Text S7 discusses the comparison between the traceability of IRHs and the “Internal-Layering Continuity Index,” an automatable proxy of IRH preservation. Finally, Text S8 describes the estimation of ice accumulation rate and vertical strain rate to H2 based on a vertical ice-flow model, and the comparison of IRH-derived to contemporary accumulation rates, as estimated by a regional climate model.

### **Text S1. Calculation of depth and fractional depth.**

We calculate IRH depth using a wave speed of  $168.5 \text{ m } \mu\text{s}^{-1}$ , a +10 m firn correction, and attach a conservative  $\pm 15 \text{ m}$  uncertainty to all IRH depths. Text S2 justifies the firn correction and Text S3 the uncertainty value. Primarily we use ice thicknesses from IMAFI as detailed by Ross et al. (2012) to calculate IRH depth as a fraction of ice thickness. In those few, inland, regions where IRHs are traced but PASIN did not image the bed during the IMAFI survey we use BedMap2 ice thicknesses (Fretwell et al., 2013). The ice thickness dataset of Ross et al. (2012) and the picks generated in this study from the Schlumberger Petrel® software are not exactly co-located. The offsets are small: up to 5 m between individual picks. In order to better visualise the spatial trends in the data over spatial wavelengths many 10s km long, and combine these datasets, we rasterised both datasets to a common 500 m grid. We then take the point in the centre of the raster grid to be representative of local properties. To test the effect of this step we perform a nearest-neighbour comparison between the interpolated, regularised picks on the 500 m grid and the nearest raw pick. For H1, H2 and H3, this results in a RMSE of 0.93, 1.53, 1.60 pixels, corresponding to a difference in IRH depth of 3.56, 5.86 and 6.13 m arising from the spatial regularisation. In dissemination of this dataset we provide both the raw picks and the regularised data. Summary statistics describing IRH depths are provided below in Table 1.

IRH	Depth below surface (m)			Depth as fraction of ice thickness		
	Mean, 1SD	Max., Min.	5 <sup>th</sup> %tile, 95 <sup>th</sup> %tile.	Mean, 1SD	Max., Min.	5 <sup>th</sup> %tile, 95 <sup>th</sup> %tile
H1	395, 73	174, 668	290, 528	0.18, 0.03	0.09, 0.41	0.14, 0.24
H2	643, 136	238, 1227	440, 857	0.31, 0.05	0.15, 0.59	0.24, 0.40
H3	841, 178	366, 1581	576, 1136	0.41, 0.05	0.22, 0.63	0.34, 0.50

**Table S1.** Summary statistics for the IRHs H1-3 picked in this study.

## Text S2. Firn correction.

Estimates of ice thickness with IPR require the addition of a “firn correction” ( $z_f$ ) to account for the higher wave speed in the less-dense near-surface layer. After Dowdeswell and Evans (2004), where  $K$  is a coefficient of 0.85,  $n_i$  is the refractive index of ice (1.78),  $\rho_i$  is the density of pure ice ( $0.917 \text{ kg m}^{-3}$ ) and  $\rho_z$  is the density at depth  $z$ ,  $z_f$  can be calculated thus:

$$z_f = \frac{K}{n_i} \int (\rho_i - \rho_z) dz \quad (\text{S1}).$$

Using density profiles from three contrasting glaciological environments, Dowdeswell and Evans (2004) reported firn corrections of 7 m on Ross Ice Shelf, 10 m in central Greenland and 15 m at Vostok. Using this method, Cavitte et al. (2016) estimated 13.60 m at Vostok and 14.60 m at Dome C. In Dronning Maud Land, Steinhage et al. (2001) applied a  $z_f$  of 13 m based on five 150 m cores. Studies in West Antarctica have typically applied a 10 m firn correction, partly owing to the lack of ice core records in West Antarctica (e.g. Vaughan et al., 2005; Ross et al., 2012).

We use data from the ice core at WAIS Divide ( $79.47^\circ\text{S}$ ,  $112.09^\circ\text{W}$ ; WD2014) to calculate  $z_f$ . The WD2014 site is  $\sim 320$  km to the nearest picked IRH from this study. Here, Kreutz et al. (2011) provide a high-resolution density profile from 0 - 160 m to depth. The upper 2 m of this core are disturbed by drifting due to drilling activities and density measurements in this section have a strong positive bias. To remove this effect, we fit a polynomial to measurements from 2-8 depth and replace measurements at 0–2 m with estimated values. At 160 m  $\rho_i$  has not been reached so we fit a linear trend from 120 m to 160 m depth and extend this with depth until  $\rho_i$  is reached at 191 m. We then resample the irregularly spaced measurements to a 0.01 m grid and calculate  $z_f$  using the complete density profile. This results in a  $z_f$  of 9.4 m at WD2014.

With this information we decided to apply a spatially invariant  $z_f$  of 10 m to our IRH depths. As the IMIS catchments span from the ice divide to the grounding line, we expect that  $z_f$  will vary from  $\sim 10$  m at the ice divide to  $\sim 7$  m close to the ice shelf. We have no reliable method for calculating this variation. Given the full range of IRH depths we image (approximately 250-1600 m depth) a variation of 3 m across the catchment is minor, but we attach a  $\pm 3$  m error to these values arising from  $z_f$ . Furthermore, a spatially invariant  $z_f$  is easily removed for follow-on work wishing to recalculate IRH depths using, for example, a firn densification model or an arbitrary elevation-based correction.

### **Text S3. Uncertainties in IRH depth.**

The uncertainties in the IRH depth arise from the firn correction, variations in the electromagnetic-wave velocity and the properties of the IPR system used. In this section we aim to estimate a reasonable maximum uncertainty of our traced IRH depths. As detailed previously the estimated error arising from the firn correction is  $\pm 3$  m. Electromagnetic-wave velocity in ice varies from 168 to  $169.5 \text{ m } \mu\text{s}^{-1}$  depending on ice temperature, fabric and impurity content (Fujita et al., 2000). For the deepest traced IRH in our dataset this results in a maximum variation of IRH depth of 14 m. The uncertainty in IRH depth owing to the IPR system is a function of its range-resolution, and the signal-to-noise ratio (SNR) of each individual IRH reflection (Cavitte et al., 2016). Following Winter et al., (2017; their Table 1) the range-resolution of PASIN IPR is 10.7 m (chirp mode) and 8.4 m (pulse mode). We do not calculate the SNR of traced reflection because our gain and amplitude normalisation routine (see Methods) removes meaningful radiometric information from the radargram, in favour of IRH visibility. To still consider this uncertainty, however, we look to IRH measurements from the University of Texas HiCARS IPR system which has a similar bandwidth and range resolution to PASIN. When tracing IRHs deeper than ours (i.e. likely with a lower SNR) in East Antarctica, Cavitte et al. (2016) quote that the precision of the range estimate varies between 0.90 and 3.87 m for this system. As PASIN operates with a slightly lower range resolution than HiCARS (8.6 m) we adopt an error arising from the IPR system as  $\pm 4$  m. If we assume that these errors are not correlated this implies a combined maximum uncertainty in IRH depth of  $\pm 15$  m.

### **Text S4. Intersections with previously dated IRHs.**

In this section we describe the comparison of the IRHs identified in this study with two previously published and dated IRHs which intersect IMAFI (see Fig 1a in the main paper). At I-1 ( $81.82^\circ\text{S}$ ,  $97.85^\circ\text{W}$ ) and I-2 ( $82.12^\circ\text{S}$ ,  $96.26^\circ\text{W}$ ) our IRHs intersect with IRHs dated from the Byrd Ice Core (Siegert and Payne, 2004; Siegert et al., 2005). At I-3 ( $83.56^\circ\text{S}$ ,  $104.97^\circ\text{W}$ ) our IRHs intersect with an unusually bright IRH identified and dated to 17.5ka by Jacobel and Welch (2005).

At I-1 and I-2 the Siegert et al. (2005) IRHs are posted at 2-3 km spacing, resulting in measurements being  $\sim 1$ -2 km from the actual point of intersection. To derive IRH depth at the intersection point we linearly interpolated from the IRH depth measured at either side; between these two points IRH depth varied up to 200 m. Additionally, the 1970s SPRI-NSF-TUD dataset has navigational uncertainties of up to several km as it was obtained before GPS location was available. As such we treat IRH depth at I-1 and I-2 as

indicative, cognisant that there may be inaccuracies of, potentially, ~100 m in IRH depth. The ITASE 2002 survey data by Jacobel and Welch (2005) provides a sounding location every ~12 m. We use our raw along-track data, which also provides a sounding location every ~10 m. IRH depths at each of these intersection sites are shown in Table 2.

Site	This study			Siegert and Payne (2004)				Jacobel and Welch (2005)
	H1	H2	H3	L07 / 3.1 ka	L10 / 5.6 ka	L11 / 6.4 ka	L12 / 16 ka	17.5 ka
I-1	357.2 ± 15	612.5 ± 15	825.9 ± 15	339.3 ± 40	598.5 ± 40	764.5 ± 40	1111.9 ± 40	1906 ± 10
I-2		571.6 ± 15	768.0 ± 15	350.1 ± 40	623.5 ± 40		1107.5 ± 40	
I-3	384.5 ± 15							

**Table 2.** IRH depths (m below ice surface) at four crossover sites. Uncertainties for Siegert and Payne (2004) and Jacobel and Welch (2005) as quoted by those studies.

### Text S5. Age-depth modelling.

We use the one-dimensional Dansgaard and Johnsen (1969) age-depth model to estimate the age of our IRHs. In this model the ice age,  $t$ , in years is given by:

$$t = \frac{(2H-h)}{2a} \ln \left( \frac{(2H-h)}{(2y-h)} \right), \quad h \leq y \leq H \quad (\text{S2})$$

where  $H$  is ice thickness (m);  $h$  is the thickness of the basal shear layer (m);  $a$  is the average accumulation (in ice equivalent  $\text{yr}^{-1}$ ); and  $y$  is height above the bed. This steady-state model was developed for use at ice divides, where ice velocity has no horizontal component, and therefore does not account for divide migration or the associated complexities of ice flow arising from anisotropic rheology. The advantage of this particular model is its simplicity, and ability to be driven largely by accumulation to independently validate IRH ages. We note, however, that more developed models allow for the interpretation of dated-IRH depth patterns (MacGregor et al., 2016; Text S8).

To apply this model, we identified a point where the IMAFI survey crosses an ice divide, all three picked IRHs are identified, the ice is as thick, and the bed as flat as possible. Site D-J on the Institute-Kamb ice divide (Site D-J on Fig. 1; 101.00°S, 81.98°W) fitted the criteria. Furthermore, this site is, relative to the rest of the IMAFI survey, close to the WD2014 site (340 km) for which the accumulation history has been published (Fudge et al., 2016). At Site D-J the calculated IRH depths are  $H1 = 436 \pm 15$  m;  $H2 = 733 \pm 15$  m; and  $H3 = 933 \pm 15$  m, and  $H$  is 2670 m ( $\pm \sim 25$  after Ross et al., 2012). The basal shear layer thickness ( $b$ ), where the ice deformation profile is no longer logarithmic, is unknown. Basal shear layer thickness has a smaller effect on modelled age than accumulation. Fahnestock et al. (2001) and Siegert and Payne (2004) used 400 m, whereas Karlsson et al. (2014) applied a range from 100-1200 m. We adopt a similar approach to Karlsson et al. (2014) and calculated  $t$  using a range of  $b$  values.

This model requires a single, average accumulation value to the IRH being dated, which must account for the variable accumulation through time at a site. Accumulation has generally been higher than present at WD2014 since  $\sim 6$  ka (Fudge et al., 2016), and the accumulation pattern close to the WD2014 site has been steady throughout the Holocene (Koutnik et al., 2016). However, Karlsson et al. (2014)'s results suggested that a change in accumulation pattern occurred in the Pine Island Glacier Southern Basin during the Holocene. Intersections with the SPRI-NSF-TUD IRHs of Siegert and Payne (2004) at I-1 suggest an approximate age for H1, H2 and H3 of 3.1 ka, 5.6 and 6.4 ka respectively (Figure 3 in main paper).

A key question is whether accumulation at WD2014 is comparable to Site D-J. To address this, we compare contemporary accumulation rates between the two sites. Mean modelled SMB 1979-2016 from the RACMO2.3 regional climate model (van Wessem et al., 2018) at Site D-J and at WD2014 is 174 and 173  $\text{kg m}^{-2} \text{yr}^{-1}$ , which translates to 0.189 and 0.190 m ice equivalent  $\text{yr}^{-1}$ . SMB as estimated from field-measurement interpolation and AMSR-E polarisation (Arthern et al., 2006) at Site D-J and at WAIS Divide are 162 and 209  $\text{kg m}^{-2} \text{yr}^{-1}$  respectively, which translates to 0.177 and 0.228 m ice equivalent  $\text{yr}^{-1}$ . Given approximate IRH ages, we calculate the mean advection-corrected ice-accumulation rate from Fudge et al. (2016) since 7, 5 and 3 ka to be 0.24, 0.25 and 0.25 ice equivalent  $\text{yr}^{-1}$ , respectively.

This indicates that average ice accumulation since IRH deposition was likely higher than modern day, but also that accumulation at WD2014 is likely larger than at Site D-J. With this, we arrive at a range of realistic accumulation values to use as inputs to our age-depth model: 0.15, 0.20, and 0.25 m ice equivalent  $\text{yr}^{-1}$ . The results of the age-depth model are shown in Tables S3-S5 and suggest ages of H1 as 1.9-3.2 ka; H2 as 3.5-6.0 ka; and H3 as 4.6-8.1 ka. We derive an empirical error estimate of between  $\pm 2.5$  and 4% for each modelled age, that arises from the uncertainty of IRH depths and ice thickness ( $H$ ), by running the

model with these values over- and under-estimated by their uncertainty ( $\pm 15$  for IRH depths and  $\pm 25$  for  $H$ ).

a, accumulation (m ice equiv. yr <sup>-1</sup> )	h, basal shear layer thickness (m)				
	200	400	600	800	1000
0.15	3185	3198	3212	3228	3245
0.20	2389	2398	2409	2421	2434
0.25	1911	1919	1927	1937	1947

**Table S3.** Age estimates ( $t$ , years) of H1 for varying accumulation ( $a$ ) and basal shear layer thicknesses ( $h$ ).

a, accumulation (m ice equiv. yr <sup>-1</sup> )	h, basal shear layer thickness (m)				
	200	400	600	800	1000
0.15	5753	5797	5846	5901	5963
0.20	4315	4348	4385	4426	4472
0.25	3452	3478	3508	3541	3578

**Table S4.** Age estimates ( $t$ , years) of H2 for varying accumulation ( $a$ ) and basal shear layer thicknesses ( $h$ ).

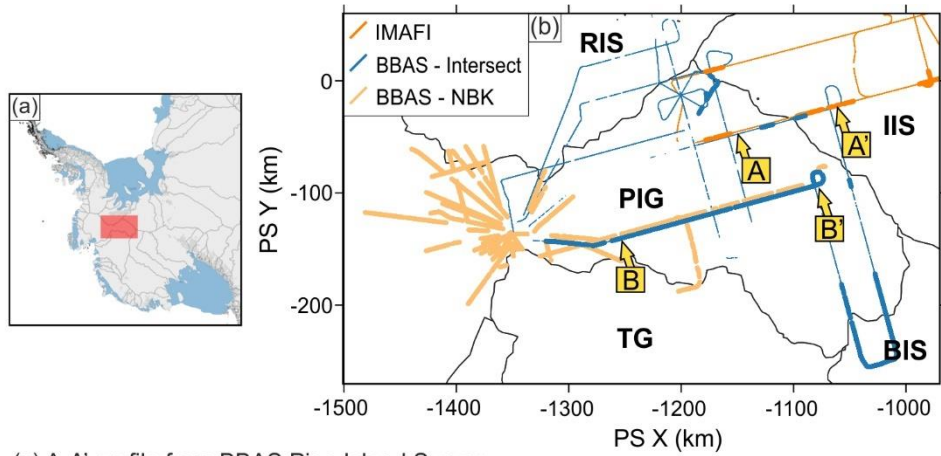
a, accumulation (m ice equiv. yr <sup>-1</sup> )	h, basal shear layer thickness (m)				
	200	400	600	800	1000
0.15	7728	7812	7905	8011	8131
0.20	5796	5859	5929	6008	6098
0.25	4637	4687	4743	4807	4878

**Table S5.** Age estimates ( $t$ , years) of H3 for varying accumulation ( $a$ ) and basal shear layer thicknesses ( $h$ ).

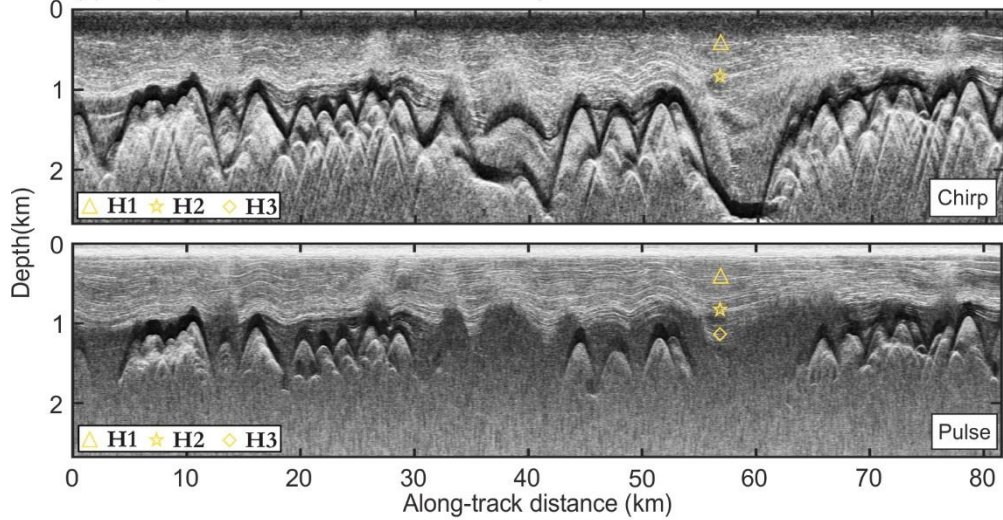
## **Text S6. Relationship to Karlsson et al. (2014) layers.**

Karlsson et al. (2014) identified a “layer package” of distinct IRHs within Pine Island Glacier using BBAS PASIN data acquired in chirp mode only. The IRHs, “L1” and “L2”, identified in that study do not intersect directly with ours (Figure 1, main paper). This raises the question of how our package of distinct IRHs focused on the IMIS region is related to theirs, and whether our H1, H2 or H3 are equivalent to their L1 or L2.

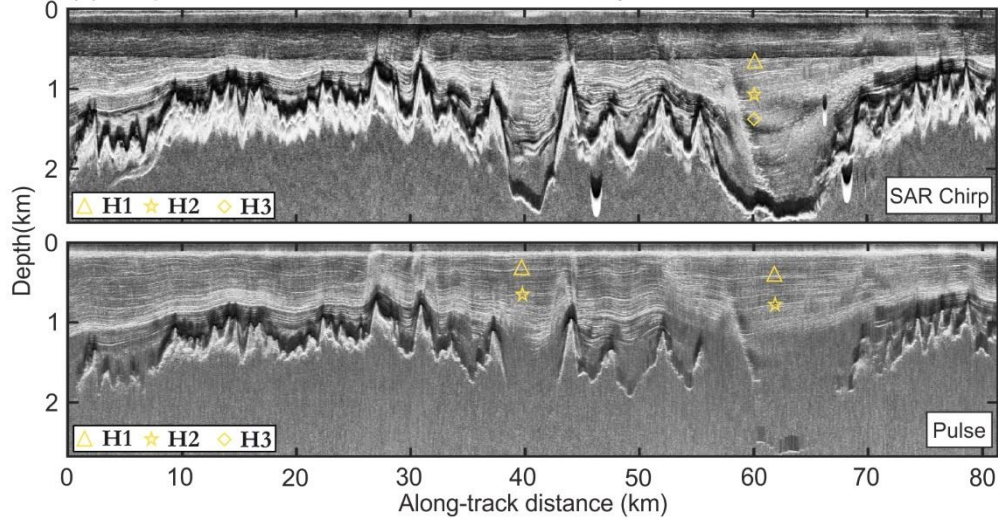
To address this, we plot three BBAS survey lines which intersect with the IMAFI survey (Figure S1), and process both the chirp and pulse mode data with the same custom gain function we derived for IMAFI. We focus on two flight sections: A-A' and B-B' (see Figure S1). At A-A' IMAFI and BBAS survey lines fly quasi-parallel to one another, laterally offset by  $\sim 2$  km. Here, we identify H1, H2 or H3 in both BBAS and IMAFI, but Karlsson et al. (2014) had not identified L1 or L2. Qualitatively we see similar patterns of IRHs in the BBAS pulse and chirp, and in the IMAFI pulse and chirp (Figure S1a and S1b). Along B-B', well away from the IMAFI survey, both we and Karlsson et al. (2014) identify some part of our IRH-packages in BBAS. By resampling both sets of picks onto a regular 10 m spaced vector along B-B' we can directly compare H1, H2 and H3 to L1 and L2. H1 shows no relation to L1 or L2, but there is considerable evidence that our H2 is equivalent to L1 and our H3 is equivalent to L2 (Figure S2). In both comparisons the  $R^2$  value is  $>0.99$  and the RMSE is 6.5 m and 5.4 m respectively. This is well within the estimated uncertainties of our IRH depths of  $\pm 15$  m (see Section S3).



(c) A-A' profile from BBAS Pine Island Survey



(d) A-A' profile from IMAFI Institute and Möller Survey



(e) B-B' profile from BBAS Pine Island Survey

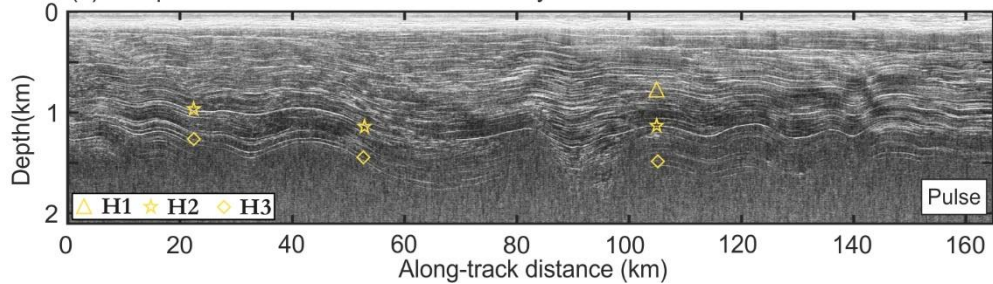


**Figure S1.** Comparison of IRHs identified in this study with intersecting flights from the 2004/05 PASIN survey of Pine Island Glacier (“BBAS”; Vaughan et al., 2006), and the “layer package” of Karlsson et al. (2014). (a) extent of panel b. (b) Survey lines of IMAFI and BBAS, thicker lines indicate that IRHs were picked in that section. Extent of picks from Karlsson et al. (2014) and ice catchments are also shown. Abbreviations as in Figure 1a. (c-d) Section A-A’ parallel radargrams from IMAFI and BBAS along A-A’ offset by ~2 km demonstrating the same IRH pattern in all four datasets. (e) Section B-B’ only flown with BBAS, showing the distinct H1-H3 pattern in the pulse mode dataset.

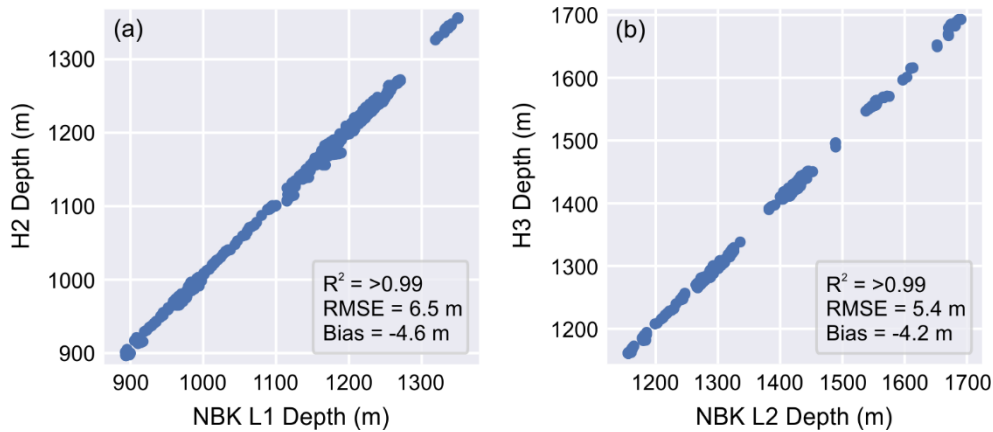


**Figure S2.** Scatter plot demonstrating the strong correlation between L1 and L2, identified by Karlsson et al. (2014), and H2 and H3 identified in this study, along B-B’ in Figure S1.

### Text S7. Relationship between Internal-Layering Continuity Index and traceability.

The Internal-Layering Continuity Index (ILCI) is an efficient automatable measure of the amount of reflected energy within a radar trace, and high ILCI values have been shown to be indicative of the presence of well-preserved IRHs (Karlsson et al., 2012). In order to test quantitatively whether ILCI could be used as an indicator of manual *traceability* in other areas we compare ILCI from IMAFI (after Bingham et al., 2015) in regions where either H1, H2 or H3 were traced with areas where they were not. The mean ILCI ( $\pm 1$  SD) where any one of these IRHs could be traced was  $0.066 \pm 0.022$ , whereas it was  $0.049 \pm 0.015$  where IRHs could not be traced (Figure S3). A Welch’s t-test, which allows for different sample sizes and variances, demonstrates that these means are statistically different ( $p$  value  $< 0.001$ ). This confirms that a high ILCI indicates where individual IRHs could be traced manually.

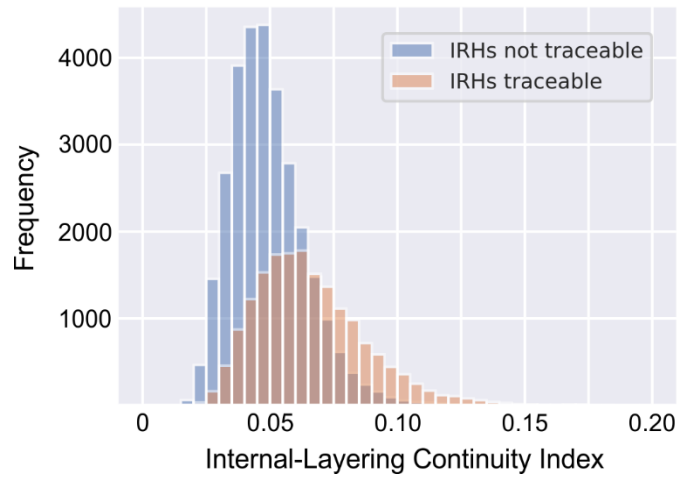


**Figure S3.** Histogram demonstrating the difference in Internal-Layering Continuity Index (ILCI) where IRHs could be traced and where they could not. The mean ILCI ( $\pm 1$  SD) where any one of these IRHs could be traced was  $0.066 \pm 0.022$ , whereas it was  $0.049 \pm 0.015$  where no IRH could be traced.

#### Text S8. Estimating palaeo-accumulation rates.

SMB is likely a control on the depth of IRHs. Figure S4 qualitatively shows a broad association between H2 depth and 1979-2016 mean SMB as estimated by a regional climate model (van Wessem et al., 2018).

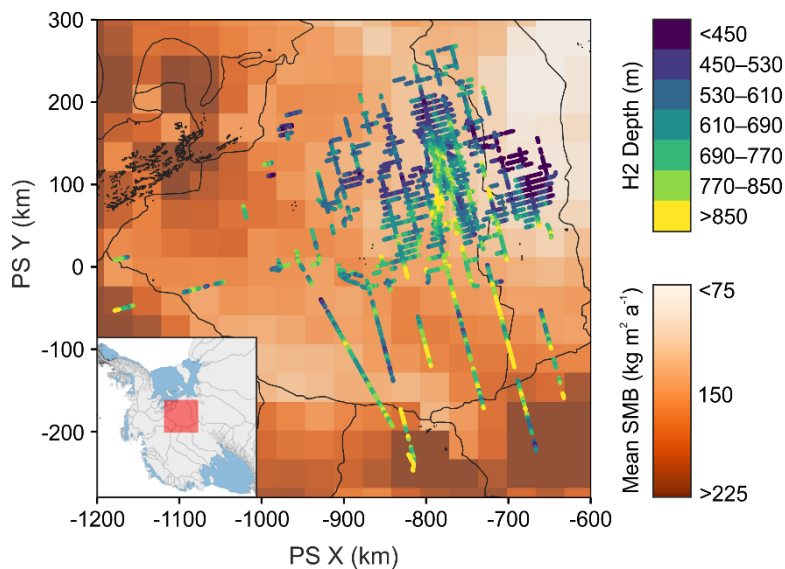


**Figure S4.** Map to demonstrate the spatial correspondence between gridded mean SMB (1979-2016) from the RACMO2.3Ant regional climate model (van Wessem et al., 2018) and depth of our most extensive IRH, H2.

To investigate to what extent SMB (often expressed as palaeo-ice-accumulation) is responsible for the broad scale pattern in IRH depth, we use a recent 1D ice flow model to estimate mean annual accumulation and mean annual vertical strain rate over the last  $\sim 5.6$  ka across the IMIS survey area (MacGregor et al., 2016). With the assumption of the local layer approximation (Waddington et al., 2007) and steady state, MacGregor et al. (2016) relate age ( $a$ ) and depth ( $z$ ) to the mean vertical strain rate ( $\dot{\epsilon}_\alpha$ ) and mean accumulation rate ( $\dot{b}_\alpha$ ) by:

$$a(z) = \frac{1}{\dot{\epsilon}_\alpha} \ln \left( \frac{\dot{b}_\alpha + \dot{\epsilon}_\alpha z}{\dot{b}_\alpha} \right). \quad (\text{S3})$$

For a set of  $N$  dated IRHs at a particular location, with the  $i$ -th IRH of an observed age ( $a_{obs}^i$ ) with an uncertainty  $\tilde{a}_{obs}^i$  and modelled age ( $a_{model}^i$ ), the apparent  $\dot{\epsilon}_\alpha$  and  $\dot{b}_\alpha$  can be found by minimising a chi-square statistic ( $\chi^2$ ):

$$\chi^2 = \sum_{i=1}^N \left( \frac{a_{obs}^i - a_{model}^i}{\tilde{a}_{obs}^i} \right)^2. \quad (\text{S4})$$

MacGregor et al. (2016) use a minimum of 4, and over 24 in some regions, well-dated IRHs to constrain  $\dot{\epsilon}_\alpha$  and  $\dot{b}_\alpha$ . In our study we use only H1 ( $3.1 \pm 0.160$  ka) and H2 ( $5.6 \pm 0.175$  ka), which can be relatively unambiguously related to IRHs dated at Intersection-1 (see Figure 3), and these, as yet, lack a detailed linking to a modern ice-core chronology.

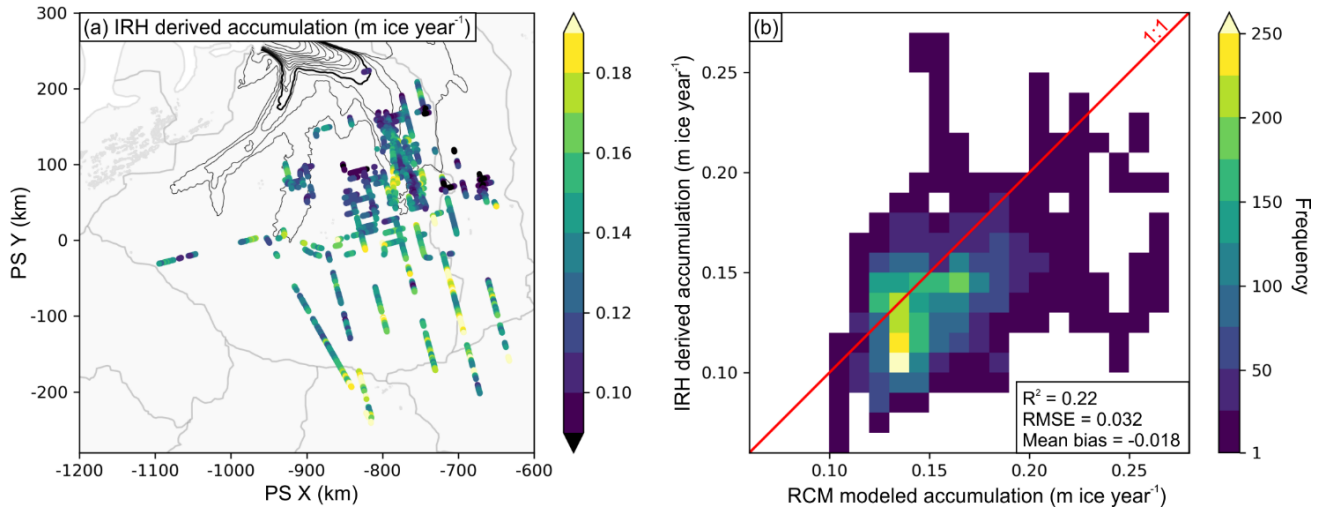


**Figure S5.** (a) Apparent IRH-derived modeled accumulation using the vertical ice flow model of MacGregor et al. (2016). (b) IRH-derived accumulation using MacGregor et al. (2016) compared to modeled SMB (1979-2016) from the nearest RACMO2.3Ant regional climate model (RCM) node (van Wessem et al., 2018). Extent as in Figure 2.

Figure S5a suggests that the accumulation rate gradient explains the broad pattern of IRH depth. Figure S5b shows that across IMIS, there is a relatively good agreement between RCM and IRH-derived accumulation results. This disagrees with ice core-based findings of a higher mean accumulation over the late Holocene at WD2014 (Fudge et al., 2016; Text S5). This may be because we are unable to constrain the model sufficiently well in this implementation. More robustly dating our horizons would improve model performance. If the assigned dates are revised to be younger after reassessment IRH-based estimates of accumulation will be larger and more consistent to those at WD2014.